GaN and AlGaN/AlN nanowire ensembles for ultraviolet photodetectors: effects of planarization with hydrogen silsesquioxane and nanowire architecture

Elçin Akar, Ioanna Dimkou, Akhil Ajay, Eric Robin, Martien Ilse den Hertog, Eva Monroy

GaN and AlGaN/AlN Nanowire Ensembles for Ultraviolet Photodetectors: Effects of Planarization with Hydrogen Silsesquioxane and Nanowire Architecture

Elçin Akar[†,*], Ioanna Dimkou[‡], Akhil Ajay[†], Eric Robin[ξ], Martien Ilse den Hertog[§], and Eva Monroy[†]

[†] Univ. Grenoble-Alpes, CEA, Grenoble INP, IRIG, PHELIQS, 38000 Grenoble, France
[‡] Univ. Grenoble-Alpes, CEA, LETI, 38000 Grenoble, France
[ξ] Univ. Grenoble-Alpes, CEA, IRIG, MEM, 38000 Grenoble, France
[§] Univ. Grenoble-Alpes, CNRS, Grenoble INP, Institut Néel, 38000 Grenoble, France

* Corresponding author: elcin.akar@cea.fr

OrcID:
Elçin Akar: 0009-0002-4221-3357
Ioanna Dimkou: 0000-0002-6865-3820
Akhil Ajay: 0000-0001-5738-5093
Eric Robin: 0000-0002-5596-2640
Martien Ilse den Hertog: 0000-0003-0781-9249
Eva Monroy: 0000-0001-5481-3267

Abstract

The interest in nanowire photodetectors stems from their unique properties, such as high sensitivity, fast response times, and compatibility with integrated circuit technology, making them well-suited for diverse application domains, including solar cells, cameras, biomedical sensors, and communication systems. Implementing devices based on nanowire ensembles requires a planarization process which must be conceived to preserve the advantages of the nanowire geometry. This is particularly challenging in the ultraviolet (UV) range, where spin coating with hydrogen silsesquioxane (HSQ) appears as an interesting approach in terms of transmittance and refractive index. Here, we report a comprehensive study on UV photodetectors based on GaN or AlGaN/AlN nanowire ensembles encapsulated in HSQ. We show that this material is efficient for passivating the nanowire surface, and it introduces a compressive strain in the nanowires and preserves their radiative efficiency. We discuss the final performance of planarized UV photodetectors based on three kinds of nanowire ensembles: (i) non-intentionally-doped (nid) GaN

nanowires, (ii) Ge-doped GaN nanowires, and (iii) nid GaN nanowires terminated with an AlGaN/AlN superlattice. The incorporation of the superlattice allows tuning the spectral response with bias, which can enhance the carrier collection from the AlGaN/AlN superlattice or from the GaN stem. In all the cases, the performance of the planarized devices remains determined by the nanowire nature, since their characteristics in terms of linearity and spectral selectivity are closer to those demonstrated in single nanowires than those of planar devices. Thus, the visible rejection is several orders of magnitude and there is no indication of persistent photocurrent, which makes all the samples suitable for UV-selective photodetection applications.

Keywords: Photodetector, ultraviolet, GaN, nanowire, superlattice, planarization, photoconductor, photodiode

1. Introduction

The market demand for reliable and high-quality detection of ultraviolet (UV) radiation keeps steadily increasing owing to its use in application domains, including pollution monitoring, industrial safety, flame detection, missile tracking, biomedical diagnosis, and space communication.[1–3] Such a trend has led advancing research on the UV photodetectors to improve the device performance with innovative ideas.[4–11] A high-performance photodetector should satisfy the "5S" requirements: high *sensitivity*, high *signal-to-noise ratio*, high spectral *selectivity*, high *speed*, and high *stability*.[12] Silicon-based detectors are widely used due to their well-developed and low-cost technology for device fabrication. However, their spectral selectivity relies on the use of filters, which are bulky and present lifetime issues.[13] With direct bandgap and the possibility to control n- and p-type doping, III-nitrides have emerged as excellent materials for the development of high-performance UV photodetectors with a spectral cut-off in the 200-400 nm range.[4,14–17] Depending on the specifications, various photodetection mechanisms can be exploited ranging from photoconductor, Schottky photodiode, p-n and p-i-n junction photodiodes, and avalanche photodiodes to metal-semiconductor-metal photodiodes by modifying the device architecture.

The nanowire geometry has opened new perspectives in the field of photodetection.[14,18] It is a promising approach since such structures can be grown almost defect-free with a high surface-to-

volume ratio. During growth, the strain relaxation along the surface can prevent dislocation formation. Recently, the performance of single-nanowire devices has been investigated in detail.[9,19] Single-nanowire photoconductors are characterized by high photocurrent gains, which can reach 10^6, and strong spectral contrast above and below the bandgap. A common feature in nanowire photoconductors is the fact that the photocurrent scales sublinearly with the impinging laser power, which has been shown for single GaN nanowires regardless of the presence of heterostructures.[20–24] In the case of undoped GaN nanowires, Sanford *et al.* and Spies *et al.* reported an improvement of linearity in nanowires with a small diameter (< 100 nm), which they attributed to the total depletion of the nanowires.[20,25] More recently, Cuesta *et al.*[26] studied a single GaN with an axial p-n junction. They showed that under reverse bias the effect of surface states becomes less emphasized and the responsivity increases linearly with a decay time of ~ 10 μs.

Apart from single nanowires, UV photodetectors based on nanowire ensembles are promising candidates for large-area UV photodetection.[27,28] In this case, the implementation of the top (illuminated) contact of the device requires the planarization of nanowires to ensure electrical access to multiple wires while preventing metallization of the sidewalls, which could cause the short-circuit of the active region. Planarization can be realized *in situ* by altering the growth conditions to promote lateral growth, forcing the vertically grown nanowires to merge at the top.[29–33] This method can offer an advantage in terms of optical transparency, since it eliminates the need of a semitransparent contact. However, the coalesced structure creates grain boundaries which can introduce additional defects in the structure, and the light concentration capacity due to the nanowire geometry diminishes. Additionally, coalescence requires time, resulting in a thick top layer, increasing the risk of optical loses as the active region moves away from the top surface. An alternative solution is the planarization of the nanowire ensemble *ex situ*, generally obtained by spin coating of a polymer. Different polymers have been employed as planarizing materials, such as polyimide[34,35], parylene[36,37], polydimethylsiloxane,[38,39] or hydrogen silsesquioxane (HSQ).[40–44] One of the first studies on nanowire ensembles based on a GaN p-i-n junction was performed by de Luna Bugallo *et al.*[40]. They fabricated UV photodetectors by planarizing with HSQ and using indium tin oxide (ITO) as the top contact. The device presents a visible rejection of the order of ~ 10^2 at zero bias. However, the response decreases for energies higher than 3.5 eV (≈ 354 nm) since ITO starts to absorb. Also, it shows a linear response as a function of incident power at low power levels (< 6×10^{-4} W/cm^2), yet subsequently the linearity deviates as a result of trapping/releasing

of photogenerated carriers. The photodetector decay time was measured in the order of milliseconds, and it is associated with a photoconductive gain mechanism appearing both at forward and reverse bias.[45] Another report[41] demonstrated the fabrication of photodetectors based on HSQ-planarized GaN nanowire ensembles using few-layered graphene as a transparent electrode. Similar to the previous example, the device shows linear behavior at low power and becomes sub-linear with increasing power density. The device achieves a responsivity value of 25 A/W under 1 V at 357 nm; unfortunately, no time response analysis was reported on this device. Furthermore, Aiello *et al.*[36] utilized parylene polymer for the planarization of InGaN/GaN disk-in-nanowire ensembles, showing photodetectors that exhibit rise and decay time responses of 190 and 454 s respectively. So far, planarization was considered a part of the fabrication process, but there is little analysis (if any) of the effect of the planarizing material on the optical properties of the nanowires and device performance. This is a relevant question to assess to what extent the advantages of single-nanowire photodetectors can be extended to devices based on arrays of nanowires.

In this study, we discuss the effect of planarization with HSQ on the optical properties of GaN nanowires, and we report a fabrication process for planarized UV photodetectors based on GaN nanowire ensembles. The process is applied to three different nanowire samples grown by plasma-assisted molecular beam epitaxy, including undoped and Ge-doped GaN nanowires, and GaN nanowires terminated with an AlGaN/AlN superlattice, to shift the spectral response to shorter wavelengths. The devices are investigated in terms of linearity, responsivity, spectral selectivity, frequency dependence, and time response. The results demonstrate that devices based on nanowire ensembles present characteristics that are closer to those of single nanowires rather than to planar structures. In particular, they maintain excellent spectral selectivity and faster response time than planar photoconductors.

2. Experimental Section

2.1. Samples under Study. In this work, we discuss the photodetector fabrication process and final performance of a set of three kind of nanowire ensembles: **SGaN** consisting of 1 μm-long non-intentionally-doped GaN nanowires, **SGaNGe** consisting of 1 μm-long GaN nanowires

doped with Ge, and GaN nanowires terminated with an $Al_{0.1}Ga_{0.9}N$/AlN superlattice referred to as **SSL**. A scheme of the three samples is presented in Figure 1a.

2.2. Growth of Self-Assembled GaN Nanowires. Self-assembled GaN nanowires were synthesized on n-type Si(111) substrates using plasma-assisted molecular beam epitaxy, following the catalyst-free technique first demonstrated by Kishino and Calleja.[46,47] The substrate was degreased using dichloromethane, acetone and methanol before baking it *in situ* at 880°C to remove the native oxide. To minimize the nanowire tilt and the residual planar growth, the process started with the deposition of a low-temperature AlN buffer layer consisting of 1.2 nm deposited at 300°C followed by 8 nm at 670°C, both grown under stoichiometric conditions (Al/N flux ratio $\Phi_{Al}/\Phi_N = 1$) and with a growth rate of 450 nm/h.[48–50] Then, the substrate temperature was increased to 810°C, and the GaN nanowire growth proceeded under N-rich conditions (Ga/N flux ratio $\Phi_{Ga}/\Phi_N = 0.25$), with a growth rate of 330 nm/h. Note that the temperatures mentioned here are real surface temperatures measured with a thermocouple that is calibrated with a pyrometer. Figure 1b illustrates the growth process of the nanowires. As reported by Consonni et al.,[51] the nanowire nucleation mechanism includes different stages (see Figure 1c). First, the incoming Ga and N atoms nucleate on the AlN buffer layer. Subsequently, there is an evolution of the shape of the GaN seed, to become a nanowire, whose vertical growth is fed not only by the Ga atoms impinging on top, but also by those diffusing along the sidewalls.[51] N-type doping of the nanowires was performed by incorporating an additional Ge flux during growth,[52,53] using a Ge cell temperature that leads to $[Ge] = 10^{20}\,cm^{-3}$ in planar layers. In the specific sample under investigation, energy-dispersive X-ray spectroscopy (EDX) measurements were performed, to confirm the composition. Top-view experiments were conducted using an Ultra55 Zeiss scanning electron microscope (SEM) equipped with a Flat Quad 5060F annular detector from Bruker. The system was operated at an acceleration voltage of 5 kV, and we used a standard of pure Ge as a reference. Quantifying low concentrations of Ge in GaN through EDX is challenging due to the need to extract the small Ge signal from a relatively high background. To overcome this issue, we developed a method that uses specific windows acting as X-ray filters, enhancing the signal-to-noise ratio in the energy range corresponding to the analyzed dopants. Additionally, we established an analytical procedure for background removal based on the normalization of the spectrum to an undoped reference spectrum. We also account for matrix effects, primarily electron stopping power, backscattering, and X-ray absorption. These effects were corrected using a patented

method,[54] implemented in a custom code named IZAC. The entire procedure was validated through Mg-, Ge- and Si-doped GaN. Results were consistent with secondary ion mass spectrometry analyses, even for concentrations below 10^{19} cm^{-3}.[55,56] In this case, from measurements in 17 nanowires, we determined that the average Ge concentration was around 8×10^{19} cm^{-3}.

In the case of nanowires terminated with an AlGaN/AlN superlattice, the growth started with the same low-temperature AlN buffer layer, followed by a 900-nm-long GaN stem growth at 810°C, to improve the uniformity of the nanowire height in the ensemble.[57] The growth continued with the deposition of an 88-period $Al_{0.1}Ga_{0.9}N$/AlN (1.5 nm/ 3 nm) superlattice at the same substrate temperature. The $Al_{0.1}Ga_{0.9}N$ sections were grown under N-rich conditions ($\Phi_{Ga}/\Phi_N = 0.25$ and $\Phi_{Al} = \Phi_{Ga}/9$). The AlN sections were grown at stoichiometry. In the case of AlN, the substrate temperature is too low to promote the diffusion of atoms along the sidewalls, and only the atoms impinging directly on the wire contribute to the growth.[58] The complete superlattice was synthesized without any growth interruption.

Top-view and cross-section SEM images of the three samples under study are shown in the Supporting Information, Figure S1. The images were obtained using a Zeiss Ultra 55A microscope operated at 3-5 keV with the in-lens secondary electron detector. The aforementioned growth process leads to N-polar GaN nanowires with a density of around $6\text{-}8\times10^{9}$ cm^{-2} and an average diameter of 66±12 nm, 86±16 nm, and 100±21 nm for samples SGaN, SGaNGe, and SSL respectively.

A detailed view of the superlattice in sample SSL is presented in the Supporting Information, Figure S2. High-angle annular dark-field (HAADF) scanning transmission electron microscopy (STEM) studies were performed using a Jeol Neo Arm working at 200 kV equipped with a probe aberration corrector.

2.3. Device Fabrication. To planarize the nanowire ensembles, FOx-25 resist (also known as HSQ) was deposited using the spin coating technique at 5000 rpm for 1 min, which leads to a nominal thickness of around 580 nm on a flat surface. Details on the effect of the spinning speed on the thickness and penetration behavior of HSQ are given in the Supporting Information, Table S1 and Figure S3. Subsequently, the spin-coated sample was pre-baked at 180°C for 5 min on a hotplate, and then annealed at 600°C in a N_2 atmosphere for 1 h. During annealing, the Si-H

bonds dissociate whereas siloxane (Si-O-Si) bonds form and HSQ transforms into SiO_x, mostly considered as silica (SiO_2) due to its network-like structure.[59]

To expose the tips of the planarized nanowires, HSQ was etched in an inductively coupled plasma - reactive ion etching (ICP-RIE) Oxford Plasmalab System100 using $CF_4/Ar/CH_2F_2$ (20/50/5 sccm) chemistry, with a radio-frequency power of 500 W and a gas pressure in the chamber of 12 mTorr, attaining an etching rate of 35 nm/min. The back contact of the devices was formed by electron beam evaporation of Ti/Au (50 nm/150 nm) directly on the back side of the Si substrate. The front contact was defined by optical lithography and electron beam evaporation of Ti/Au (50 nm/150 nm). The last step was to deposit a semitransparent (7.5 nm) Au layer by optical lithography and electron beam evaporation on the already-defined top contact pattern.

The morphological properties of the samples were probed throughout the device fabrication process using SEM and atomic force microscopy (AFM). For AFM images, we used a Bruker Dimension Icon system equipped with TESPA-V2 tips from Bruker, which operated in the tapping mode.

2.4. Optical Spectroscopy. The photoluminescence (PL) setup used for this study includes a frequency-doubled solid-state Ar^+ laser emitting at 244 nm. The photons emitted from the sample were studied using a Jobin Yvon HR460 monochromator coupled with a liquid-nitrogen-cooled UV-enhanced charge-coupled device (CCD) camera. The PL experiments were carried out at 5 K to reduce the influence of phonons or thermally activated non-radiative processes. The samples were mounted on a cold finger of a He cryostat.

2.5. Opto-Electrical Characterization. Current-voltage (I-V) measurements were conducted using an Agilent 4155C semiconductor parameter analyzer connected to a probe station. The validated devices in each sample were wire bonded on the ceramic chip which was then mounted on the custom-made sample holder. To evaluate the variation of the photocurrent as a function of the impinging optical power and chopping frequency, samples were excited with an unfocused continuous-wave HeCd laser (λ= 325 nm) with a spot diameter of 1 mm. For the power dependence measurements, the laser was chopped at 90 Hz and the devices were connected in series with a power supply and a Stanford Research Systems SR 830 lock-in amplifier. Depending on the device response, the lock-in amplifier is connected through a $\times 10^6$ V/A transimpedance amplifier or used as a voltmeter. In the latter case, it measures the voltage drop in a load resistor

(10 or 100 kΩ) connected in series with the photodetector. The same setup was connected with a TDS2022C oscilloscope in series to characterize the time response of the devices by measuring the voltage drop in the load resistance. The spectral response of the devices was characterized exciting them with a 450 W Xe lamp coupled with a Gemini 180 Jobin-Yvon grating monochromator. All the electrical and photocurrent studies were performed at room temperature.

3. Results

3.1 Device Fabrication Choices: Justification and Impact. The device fabrication process, schematically described in Figure 2, consists of the following steps: planarization of the nanowire ensembles, etching to expose the upper part of the nanowires, back and front metallization, and deposition of a semitransparent spreading layer. As a first step, it is necessary to encapsulate the nanowires in an insulating material with good wetting properties, to reduce the risk of metal evaporation between the nanowires creating shunt paths.[60] Ideally, the planarizing material should also be able to passivate surface states.[36] Furthermore, to preserve the optical advantages of the nanowire geometry, it is important that its refractive index is lower than the refractive index of the nanowires, and it must be transparent at the operation wavelength of the device.

In this study, we used the FOx-25 resist to encapsulate the nanowires. FOx (flowable oxide), also known as HSQ, is a negative resist mostly employed for electron-beam lithography with favorable mechanical stability, good dielectric properties and high gap-filling behavior.[40] HSQ was deposited using the spin coating technique, and annealed to form silica (see the Device Fabrication section). With a refractive index in the range of 1.55 to 1.4,[16] to be compared with 2.52 for GaN at 400 nm,[61] and excellent transmittance in the UV range, silica fulfills the optical requirements for this application.

Since the transparency in the UV range of the planarizing material is determining for the device performance, the optical transmittance was verified experimentally: a sapphire wafer was spin-coated with HSQ at 3000 rpm for 60 s (HSQ layer thickness = 695 nm) followed by annealing at 700°C in N_2 atmosphere for 1 h. The transmission was tested using a HeCd laser with $\lambda = 325$ nm at normal incidence, using uncoated sapphire as a reference. The optical transmission losses were negligible within the error bar of the measurements. Considering the planarization of SGaN

nanowires, Figure 3a shows an SEM image of the cross-section and an AFM image of the top surface of SGaN after spin-coating. HSQ fills the gap between nanowires and offers a flat top surface with a root-mean-square (RMS) roughness of 0.78 nm, measured in 1×1 μm^2. The total HSQ thickness of the coated sample is larger than the nominal HSQ thickness on a flat substrate (see the Supporting Information, Table S1), revealing that the nanowire shape and density obstruct HSQ spreading. In this regard, deviations in the coating thickness are expected from sample to sample. For instance, the tapered geometry and larger diameter of the nanowires in sample SSL result in the generation of small voids during the HSQ coating, as shown in the Supporting Information, Figure S3.

Following the planarization step, dry etching was performed to expose the tip of the nanowires. Figure 3b,c shows cross-section SEM and AFM images of the SGaN sample after etching 150 nm and 350 nm. After 150 nm etching, the surface of the sample was still uniformly covered by HSQ, without major degradation of the surface roughness (RMS roughness = 0.95 nm, measured in 1×1 μm^2). After 350 nm etching, the tips of the nanowires were exposed, enabling electrical contact.

Unfortunately, it is not possible to compare the photodetector performance with and without planarization, as it is not possible to establish a top contact for the ensemble without the planarizing step. However, PL spectroscopy can be conducted before and after planarization, hence providing a means to probe the effect of HSQ on the optical properties of nanowires. From a comparative analysis of as-grown SGaN and the specimens in Figure 3b,c (coated SGaN after 150 nm etching and after 350 nm etching), we gain access to some optical and mechanical effects of coating on the nanowires. The low-temperature (5 K) PL spectra of the as-grown and gradually etched SGaN samples are displayed in

Figure ***4***. The spectrum of the as-grown sample is dominated by the donor-bound exciton transition (D^0X) at around 357 nm (Figure 4).[62,63] The free exciton A appears as a shoulder at 356 nm. In the case of the 150-nm-etched sample, with nanowires fully embedded in HSQ, the D^0X peak is blue shifted and drastically broadened. These alterations can be attributed to the inhomogeneous strain distribution in the nanowires after the planarization.[64–66] If we assume that the HSQ generates a hydrostatic pressure, a blue shift on the PL spectrum can be attributed to the fact that the strain is compressive.[66]

To assess if there is a degradation of the total light emission due to the planarization process, we calculated the integrated PL intensity in both as-grown and 150-nm-etched samples, concluding that the total intensity drops by only 33% due to the encapsulation. To investigate the origin of this drop, we need to assess also the difference in excitation. In the planarized sample, the excitation laser (244 nm wavelength) has to penetrate around 200 nm of HSQ before reaching the nanowires (see Figure 3b). Therefore, we measured the transmittance of HSQ deposited on sapphire at 244 nm. The transmission loss due to an HSQ layer with a thickness of $d_{HSQ} = 695\ nm$ was $1 - T_{opt}(\lambda = 244\ nm) = 0.84$, using uncoated sapphire as a reference. This leads to an estimation of the absorption coefficient $\alpha(\lambda = 244\ nm) = -\frac{[Ln(T_{opt})]}{d_{HSQ}} = 2.6 \times 10^4\ \text{cm}^{-1}$. The thickness of HSQ on top of the nanowires is estimated to be around 200 nm (see Figure 3b), therefore, we approximate an attenuation of the excitation laser by $1 - exp[\alpha(\lambda = 244\ nm) \times d_{HSQ}] = 0.31$, which explains the 33% decrease in the PL intensity.

Let us focus now on the spectrum of the 350-nm-etched sample. The D^0X transition is spectrally shifted towards the as-grown sample compared to the 150-nm-etched sample with an intermediate broadening of the spectrum. Such behavior is ascribed to the release of strain in the nanowires, which occurs when exposing the tips. In this case, the integrated PL intensity is 98% of the as-grown sample value. This validates that there is no optical degradation introduced in the active material due to the planarization process, and the compressive strain can be elastically released.

To complete the study of the PL spectra, a secondary peak associated with excitons bound to surface states (SX) is observed at 359 nm in the as-grown sample.[67] In both 150 and 350-nm-etched samples, this peak seems to diminish which points to successful surface passivation. Finally, a transition related to excitons bound to stacking faults (SF) is observed at 362 nm in the spectrum of the as-grown sample.[67–69] Such defects are generated in the early stages of growth of self-assembled GaN nanowires. A quenching of the SF emission after planarization is unexpected, since HSQ is presumed to not alter the structural properties of the nanowires. The fact that the SF emission is not observed in samples with HSQ is due to the fact that the stacking faults are located in the vicinity of the substrate, and the probe laser would have to penetrate deep into the structure to excite that area (at 244 nm, only 13% of light can penetrate through 1 μm of HSQ).

Once the samples were planarized and etched to expose the nanowire tips, metal pads were deposited using optical lithography and electron beam evaporation of Ti/Au. The top contact incorporates a region of 375 μm × 460 μm with a pattern consisting of 3 μm fingers with 3 μm pitch. Finally, a second lithography step is applied to deposit a 7.5-nm-thick semitransparent Au layer, to increase the number of nanowires that are contacted. A top-view image of the final devices is presented in Figure 5a. The total dimension of one device, including fingers, contact pad, and semitransparent contact, is 500 μm × 500 μm.

3.2. Electrical Characterization in the dark. Figure 5b displays typical current-voltage (I-V) characteristics of the samples in the dark, on a semi-logarithmic scale. Bias was applied to the top contact, whereas the backside contact was grounded. SGaN exhibits a nonlinear, asymmetric characteristic, displaying higher conduction for forward bias. This indicates that the top contact is rectifying. Indeed, Ti is expected to form a Schottky contact on n-type GaN, with a Schottky barrier experimentally measured to be in the range of 0.55-0.65 eV.[70] In the case of the bottom contact, outdiffusion of silicon from the substrate is expected to slightly n-dope the bottom part of the nanowires, favoring carrier exchange with the substrate via tunneling processes.

The I-V characteristic of SGaNGe shows improved symmetry and significantly higher current than that of SGaN. This is explained by the fact that Ge doping increases the nanowire conductivity and decreases the depletion region width below the top Schottky contact, which favors carrier tunneling.

Finally, the I-V curve of the SSL sample presents rectifying behavior, as expected from its asymmetric nature. The presence of the AlGaN/AlN heterostructure raises the Schottky barrier height of Ti/Au contact as well as the nanowire series resistance, which explains the significantly lower current level in this sample.

3.3. Characterization under Illumination. Figure 6 presents the photoresponse of samples SGaN and SGaNGe. The variation of the photocurrent, I_{ph}, as a function of the incident power density, P, is displayed in Figure 6a,b in log-log plots, where the slope of a linear trend is indicated with a dashed line. The measurements were performed at 325 nm using a 100 kΩ load resistance. The experimental data were fitted to a power law $I_{ph} \propto P^{\beta}$. The β values extracted from each curve are given on the graphs next to their corresponding curves.

To understand the response of the devices under illumination, we must keep in mind the difference between photoconductive devices and Schottky photodiodes. In photoconductors, there are two main mechanisms involved in the increase of conductance during illumination. On the one hand, photons generate additional free carriers, which is generally a linear process with the optical power. On the other hand, light modifies the occupancy of defect states (point defects, dislocations, and surfaces), which leads to a decrease of their capture radius, i.e. an increase of the average mobility. This latter process is strongly nonlinear and can lead to a huge gain and slow recovery times.[15] On the contrary, the photocurrent response of Schottky photodiodes is generally linear, since the variation of the photocurrent is dominated by the photogeneration and drift by the built-in electric field.[15] In the case of single-nanowire devices, most authors report a sublinear behavior with the optical power,[21] even in the case of Schottky diodes.[20,25,71] This feature is assigned to the relatively high series resistance associated with the nanowire stem, which behaves as a photoconductor in series with the photodiode. The nonlinear behavior of photoconductors is enhanced in the nanowire geometry due to the large surface-to-volume ratio. In general, a depletion layer forms due to the Fermi level pinning on the sidewalls of the nanowires, and the diameter of the conductive core depends on the illumination intensity, which modulates the charge state of the surface levels at the sidewalls.[71] Linearity is recovered in the case of nanowires that are thin enough to be fully depleted as a result of surface states.[25,71] In this case, the modulation of the occupancy of the surface states does not have any significant effect in the core of the wire, and photogeneration of carriers is the dominant detection mechanism.

Looking back to Figure 6a,b, the behavior of the two samples under bias is strongly sublinear, with the undoped sample providing a significantly higher response. This is consistent with the response of planar photoconductors.[72] In contrast with the doped sample, the undoped nanowire array behaves asymmetrically with bias, with a higher response under reverse bias. This confirms the Schottky nature of the SGaN top contact, which plays a role to enhance the carrier collection at zero bias and under reverse bias.

Let us recall here that a symmetric photoconductor should not present any photoresponse at zero bias. However, both samples present a response, which appears due to the device asymmetry (Ti/Au top contact directly on the nanowires, and back contact on silicon, requiring carriers to traverse the heterojunction). Interestingly, there is a major difference between the two samples at

zero bias: The zero-bias response of SGaN is approximately linear. Comparing with the results obtained in single nanowires,[25,71] the linearity suggests that the nanowires are fully depleted, implying that the dominant response mechanism is the photogeneration of carriers, as the variation of the surface depletion region under illumination is negligible.[25]

To validate this assumption, we calculate the critical diameter for total depletion, which can be estimated as[71,73]

$$d_{crit} = \sqrt{\frac{16\varepsilon_{GaN}\varepsilon_0\psi}{e^2 N_D}} \quad (1)$$

where $\varepsilon_{GaN} \approx 9$ is the dielectric constant of GaN, ε_0 is the permittivity of vacuum, ψ is the location of the Fermi level below the conduction band at the surface, e is the elementary charge and N_D is the net n-type dopant density. In n-type GaN nanowires, $\psi \approx 0.6$ eV, varying as a function of the environment and the illumination conditions. If we consider the average diameter of the nanowires in samples SGaN and SGaNGe (66±12 nm, and 86±16 nm, respectively), we observe that

i. SGaN should be fully depleted for $N_D < 1.1\times10^{18}$ cm^{-3}, significantly higher than the expected residual doping, and

ii. SGaNGe, with an average doping level of $N_D \approx 8\times10^{19}$ cm^{-3}, should present a depletion region that will be a thin (<10 nm) shell.

This difference explains the lower dark current and higher responsivity of SGaN, and the severe sublinearity of SGaNGe, even at zero bias."

Figure 6c displays the spectral response of the SGaN and SGaNGe at 5 V and 0 V, respectively. Note that the spectral responsivity measurement is done with a Xe lamp (lower power density than a HeCd laser); hence, the SGaN sample could not be measured at low bias due to the high noise level. However, considering the symmetry of the samples, no spectral variation with bias is expected. Both samples display a sharp cut-off around $\lambda \approx 364$ nm (i.e., GaN bandgap). The visible response remains below the noise level. This confirms that the data presented in Figure 6a,b correspond to the photoresponse of GaN nanowires, and are not influenced by the silicon substrate. Furthermore, it confirms that the devices maintain the spectral characteristics observed in single-nanowire photodetectors: a sharp spectral cut-off even in the photoconductor configuration.[21]

Planar photoconductors present a degraded spectral contrast due to the presence of extended defects generating electronic levels within the bandgap. In contrast, the main extended defect in nanowires is the sidewall surface,[15] generally *m*-{10-10} planes that do not contain mid-gap energy levels.[21] Therefore, Figure 6c shows that the spectral response of nanowire arrays is determined by the nature of the nanowire surfaces, which is not perturbed by the planarization process.

The frequency dependence of SGaN and SGaNGe was measured under a 325-nm irradiance of 10 mW/cm^2, with the results shown in Figure 6d. The graph shows the typical behavior observed in single GaN nanowire photodetectors[21], with the photocurrent decreasing with increasing chopping frequency, which confirms the presence of a detection mechanism with a slow recovery time. Consistently, the photocurrent decays measured in the oscilloscope using a 100 kΩ load resistance are in the range of 1 and 2 ms for the sample SGaN under -1 and +1 V, respectively. The faster time response under negative bias is consistent with the asymmetry observed in the I-V curve due to the Schottky nature of the top contact. On the other hand, SGaNGe shows a decay time in the range of 2 ms both under -1 and +1 V. A more detailed analysis of the photodetector decay time is given in the Supporting Information, Figure S4.

Finally, Figure 7 presents the photoresponse of the SSL sample: terminated with an AlGaN/AlN superlattice. As shown in Figure 7a, the SSL sample presents a nonlinear trend which can be attributed to the photoinduced variation of the resistance of the GaN stem that plays an important role during the carrier collection process. The spectral response of SSL under different bias is given in Figure 7b. The spectrum under zero bias shows the characteristic of GaN, which supports that mostly the GaN stem contributes to the photocurrent measurements. Yet, for forward bias higher than 1 V, a shift towards shorter wavelengths is observed, which suggests that the AlGaN/AlN superlattice dominates the response of the device.

It is interesting to correlate the observed spectral response with the frequency dependence as a function of bias, displayed in Figure 7c. As was the case for the photoconductive samples, the photocurrent decreases with increasing chopping frequency for forward bias at +3 V. However, the trend is inverted for any bias below +3 V. To understand the inversion of the trend, the photocurrent as a function of time at +3 and -3 V is given in Figure 8a,b. At +3 V, the device response exhibits rise and decay transients that are well fitted with a biexponential function. In contrast, at -3 V, the (negative) photocurrent increases sharply when the illumination is turned on,

and then decreases to a stand-by level. When light is switched off, there is a current spike in the opposite direction, and then the signal progressively decreases to the zero level. These transients are also well fitted with biexponential functions.

In the structure terminated with a superlattice, the electric fields involved in the collection of photogenerated carriers are schematically represented in Figure 8c. There is an electric field associated with the top Schottky diode (E_{Sch}), which points along the [000-1] direction. On the other hand, the internal electric fields due to the difference of polarization between the GaN stem and the superlattice ($E_{P,GaN}$ and $E_{P,SL}$) point towards the negatively charged interface, i.e. the field is [000-1]-oriented in the GaN stem and [0001]-oriented in the superlattice. To see what are the dominating fields and understand the behavior observed under positive/negative bias, one-dimensional calculations of the SSL band structure along the growth axis were performed using the Nextnano^3 software.[74,75] The results of the simulation can be seen in Figure 8d,e, under forward and reverse bias, respectively. The black band diagram corresponds to the potential profile of the nanowire structure under zero bias (the quantum wells were smoothed out in this reference profile). At zero bias, a polarization-induced negative charge sheet is formed at the interface between the GaN stem and the superlattice; hence, the bands present a triangle-shaped potential. Such polarization and the associated electric fields create a wide depletion region, so that the superlattice is almost fully depleted. Under positive bias, the depletion region shrinks towards the GaN/SL interface, the bands flatten along the GaN stem, and photogenerated carriers are collected mainly from the superlattice. Under negative bias, the space charge region extends both along the GaN stem and the superlattice, the bands flatten along the superlattice, and the carrier collection takes place predominantly from the GaN stem. The results of the band simulations are in good agreement with the spectral responsivity of the SSL sample under different bias, showing a blue shift of the response under forward bias attesting absorption in the superlattice. Such a spectral variation of the response with bias is in agreement with previous reports in single-nanowire photodetectors incorporating GaN/AlN superlattices.[76,77]

The transient behavior represented in Figure 8a,b is a manifestation of the two opposed electric fields, $E_{P,GaN}$ and $E_{P,SL}$, in areas with different carrier dynamics. Under forward bias, the electric field associated with the Schottky contact, $E_{Sch,}$ is negligible, and the carriers are collected from the superlattice, with photocurrent decay/rise times of ≈ 280 μs (measured on a 100 kΩ load

resistance). Under reverse bias, the contribution of E_{Sch} becomes more pronounced and generates a non-uniform field distribution, which may lead to a sudden increase/decrease of photocurrent during switch on/off.[78] The observed photocurrent overshoot is due to the asymmetric carrier dynamics arising from these unbalanced opposing electric fields with $E_{P,GaN}$ and E_{Sch} pointing towards the Schottky contact (positive photocurrent) and $E_{P,SL}$ pointing towards the GaN stem (negative photocurrent). SSL presents a fast rise time (< 100 μs) due to the fast reaction of the GaN stem, followed by slow relaxation (a decay time of ≈ 280 μs), due to the compensating reaction at the SL. This explanation is consistent with the observation of a higher photoresponse when the photocurrent generated in the SL is dominant (+3 V bias in Figure 7a). The SSL sample shows increased photocurrent levels with increasing chopping frequencies for any applied bias below 3 V, Figure 7c. This can be attributed to the current spike at the onset of illumination for reverse bias (Figure 8b) increasingly influencing the average photocurrent output during the increasingly short illumination period.

4. Discussion

Overall, all the devices present a visible rejection higher than two orders of magnitude due to the absence of energy levels in the bandgap at the nanowire sidewalls.[79] The spectral selectivity of these samples makes them favorable compared to commercial UV photodetectors based on Si[80] and GaP[81] photodetectors, which require filters to attain visible-blind detection. The result is also remarkably better than the UV/visible contrast obtained in planar GaN photoconductors,[15] thanks to the reduced density of grain boundaries and dislocations in self-assembled nanowires. The time response of all samples is in the range from 2 ms to few hundreds of μs, with the fastest response of ≈ 100 μs for the SSL sample. The measured device operation speeds are faster than previously reported in photodetectors based on ensembles of GaN nanowires,[31,38,40,82,83] although slower than those of ZnO single nanowires.[84] Compared with planar GaN photoconductors, which exhibit persistent photoconductivity effects that can last seconds or even hours,[15,85,86] photoconductive nanowire ensembles present a remarkably fast response. The responsivity of the samples can be estimated as $R_{ph} = I_{ph}/(PA_{dev})$, where P is the irradiance and A_{dev} is the optical area of the device. At 325 nm, for an irradiance of around 10 mW/cm^2, the responsivity at -1 V bias is 1.0, 0.2, and 0.68 mA/cm^2 for samples SGaN, SGaNGe and SSL, respectively. Note that these values depend on the illumination power, increasing with decreasing irradiance. Due to their asymmetric

nature, the responsivity of SGaN and SSL is lower under +1 V bias (0.58 and 0.21 mA/W, respectively). These responsivity values are two orders of magnitude lower than some previous reports on photodetectors based on GaN nanowire ensembles.[40,41] The relatively low responsivity values of our samples can be related to the semitransparent Au layer, which is not sufficient to collect the photocurrent from all the nanowires located between the fingers. Another reason could be the contact fingers themselves concealing a big part of the illuminated area. Different approaches to improve the responsivity can be applied, namely, the thickness of the Au layer can be increased to collect the signal from nanowires more efficiently. Another way could be the modification of the contact design to eliminate the effect of fingers on the nanowire illumination. Finally, using different contact materials such as ITO,[36,45] graphene,[28,41] two-dimensional transition metal dichalcogenides,[82] or applying a silver nanowire dispersion to enhance the wires contacted in parallel[38,83] could be interesting to further enhance the device performance.

On the other hand, the opto-electrical characterization of the samples was investigated with an unfocused continuous-wave HeCd laser emitting at λ=325 nm, whose wavelength is in the middle of the device response band. We have also verified that HSQ is partially absorbing at λ=244 nm. It would be interesting to examine the device responsivity using lasers at different UV wavelengths, to explore the spectral limits with higher precision. However, the availability of continuous-wave lasers in this spectral range is limited, and experiments performed with a pulsed laser would not be directly comparable with continuous-wave laser measurements in view of the frequency dependence observed.

Comparing the results obtained in samples SGaN and SGaNGe, we conclude that better performance in terms of responsivity and linearity is obtained using nanowires with a doping level as low as possible, to favor the complete depletion of the wire by surface states. Regarding SSL, the interest of this sample is the potential of tuning the spectral cutoff as a function of bias. This property, which had been demonstrated in single-nanowire photodetectors incorporating a superlattice,[76] is now validated in large-area devices based on nanowire ensembles. In comparison with SGaN and SGaN, the superlattice leads also to a significant reduction of the dark current, without degrading the responsivity or time response. The challenge for this architecture would be to reduce the nanowire diameter to reach the point of total depletion, which should improve the linearity of the devices.

■ Conclusions

In this paper, we have assessed the effect of the planarization on the optical characteristics of GaN self-assembled nanowire ensembles grown by catalyst-free plasma-assisted molecular beam epitaxy, with the target of fabricating large-area UV photodetectors for a variety of application domains, i.e., military missile tracking, biological sensors, communication systems, etc. Considering the wetting behavior, refractive index, and transparency in the UV range, we decided to perform our experiments with HSQ, which can efficiently fill the space between nanowires. A detailed PL analysis showed that HSQ planarization is successful for the surface passivation of nanowires and preserves the radiative efficiency, in spite of imposing a compressive mechanical strain in the structure. Using these results, we have established a photodetector fabrication protocol, and we demonstrate a comparative study of three nanowire samples, consisting of non-intentionally-doped GaN nanowires (SGaN), Ge-doped nanowires (SGaNGe), and GaN nanowires terminated with an AlGaN/AlN superlattice (SSL). All three samples show a sublinear trend as a function of the impinging optical power, the only exception being the SGaN sample at 0 V, due to its nanowire diameter being below the critical diameter for full depletion. This sublinearity is characteristic of photoconductors and non-depleted single-nanowire devices. However, planar photoconductors present persistent photoconductivity phenomena and poor UV/visible contrast. The nanowire devices described in this paper present a visible rejection higher than two orders of magnitude, which fits rather the characteristic of single-nanowire devices. The SSL structure displays spectral characteristics and dynamics that depend on bias, and that originate from the presence of opposed internal electric fields along the nanowire, due to the spontaneous polarization in III-nitride materials.

■ Supporting Information

Top-view and cross-section SEM images of the samples under study, HAADF-STEM images of the sample SSL, effect of the spinning speed on the planarization process, effect of the planarization on the sample morphology, and the photocurrent decay analysis of the samples SGaN and SGaNGe.

■ Acknowledgements

This project received funding from the European Research Council under the European Union's H2020 Research and Innovation programme via the e-See project (Grant No. 758385), and from the French National Research Agency (ANR) via the INMOST project (ANR-19-CE08-0025).

References

(1) Aggarwal, N.; Gupta, G. Enlightening Gallium Nitride-Based UV Photodetectors. *J. Mater. Chem. C* **2020**, *8* (36), 12348–12354. https://doi.org/10.1039/D0TC03219K.

(2) Zou, Y.; Zhang, Y.; Hu, Y.; Gu, H. Ultraviolet Detectors Based on Wide Bandgap Semiconductor Nanowire: A Review. *Sensors* **2018**, *18* (7), 2072. https://doi.org/10.3390/s18072072.

(3) Chen, H.; Liu, K.; Hu, L.; Al-Ghamdi, A. A.; Fang, X. New Concept Ultraviolet Photodetectors. *Materials Today* **2015**, *18* (9), 493–502. https://doi.org/10.1016/j.mattod.2015.06.001.

(4) Cai, Q.; You, H.; Guo, H.; Wang, J.; Liu, B.; Xie, Z.; Chen, D.; Lu, H.; Zheng, Y.; Zhang, R. Progress on AlGaN-Based Solar-Blind Ultraviolet Photodetectors and Focal Plane Arrays. *Light Sci Appl* **2021**, *10* (1), 94. https://doi.org/10.1038/s41377-021-00527-4.

(5) Chen, J.; Ouyang, W.; Yang, W.; He, J.; Fang, X. Recent Progress of Heterojunction Ultraviolet Photodetectors: Materials, Integrations, and Applications. *Adv. Funct. Mater.* **2020**, *30* (16), 1909909. https://doi.org/10.1002/adfm.201909909.

(6) Ouyang, W.; Chen, J.; Shi, Z.; Fang, X. Self-Powered UV Photodetectors Based on ZnO Nanomaterials. *Applied Physics Reviews* **2021**, *8* (3), 031315. https://doi.org/10.1063/5.0058482.

(7) Jia, L.; Zheng, W.; Huang, F. Vacuum-Ultraviolet Photodetectors. *PhotoniX* **2020**, *1* (1), 22. https://doi.org/10.1186/s43074-020-00022-w.

(8) Li, Z.; Li, Z.; Zuo, C.; Fang, X. Application of Nanostructured TiO_2 in UV Photodetectors: A Review. *Advanced Materials* **2022**, *34* (28), 2109083. https://doi.org/10.1002/adma.202109083.

(9) Spies, M.; Monroy, E. Nanowire Photodetectors Based on Wurtzite Semiconductor Heterostructures. *Semicond. Sci. Technol.* **2019**, *34* (5), 053002. https://doi.org/10.1088/1361-6641/ab0cb8.

(10) Xu, J.; Zheng, W.; Huang, F. Gallium Oxide Solar-Blind Ultraviolet Photodetectors: A Review. *J. Mater. Chem. C* **2019**, *7* (29), 8753–8770. https://doi.org/10.1039/C9TC02055A.

(11) Zhang, Y.; Li, S.; Li, Z.; Liu, H.; Liu, X.; Chen, J.; Fang, X. High-Performance Two-Dimensional Perovskite $Ca_2Nb_3O_{10}$ UV Photodetectors. *Nano Lett.* **2021**, *21* (1), 382–388. https://doi.org/10.1021/acs.nanolett.0c03759.

(12) Liao, M.; Sang, L.; Teraji, T.; Imura, M.; Alvarez, J.; Koide, Y. Comprehensive Investigation of Single Crystal Diamond Deep-Ultraviolet Detectors. *Jpn. J. Appl. Phys.* **2012**, *51*, 090115. https://doi.org/10.1143/JJAP.51.090115.

(13) Caria, M.; Barberini, L.; Cadeddu, S.; Giannattasio, A.; Rusani, A.; Sesselego, A.; Lai, A.; D'Auria, S.; Dubecky, F. Gallium Arsenide Photodetectors for Imaging in the Far Ultraviolet Region. *Appl. Phys. Lett.* **2002**, *81* (8), 1506–1508. https://doi.org/10.1063/1.1497996.

(14) Sang, L.; Liao, M.; Sumiya, M. A Comprehensive Review of Semiconductor Ultraviolet Photodetectors: From Thin Film to One-Dimensional Nanostructures. *Sensors* **2013**, *13* (8), 10482–10518. https://doi.org/10.3390/s130810482.

(15) Monroy, E.; Omn s, F.; Calle, F. Wide-Bandgap Semiconductor Ultraviolet Photodetectors. *Semicond. Sci. Technol.* **2003**, *18* (4), R33–R51. https://doi.org/10.1088/0268-1242/18/4/201.

(16) Razeghi, M. III-Nitride Optoelectronic Devices: From Ultraviolet Toward Terahertz. *IEEE Photonics Journal* **2011**, *3* (2), 263–267. https://doi.org/10.1109/JPHOT.2011.2135340.

(17) Varshney, U.; Aggarwal, N.; Gupta, G. Current Advances in Solar-Blind Photodetection Technology: Using Ga $_2$ O $_3$ and AlGaN. *J. Mater. Chem. C* **2022**, *10* (5), 1573–1593. https://doi.org/10.1039/D1TC05101F.
(18) Peng, L.; Hu, L.; Fang, X. Low-Dimensional Nanostructure Ultraviolet Photodetectors. *Adv. Mater.* **2013**, *25* (37), 5321–5328. https://doi.org/10.1002/adma.201301802.
(19) Li, Z.; Allen, J.; Allen, M.; Tan, H. H.; Jagadish, C.; Fu, L. Review on III-V Semiconductor Single Nanowire-Based Room Temperature Infrared Photodetectors. *Materials* **2020**, *13* (6), 1400. https://doi.org/10.3390/ma13061400.
(20) Sanford, N. A.; Blanchard, P. T.; Bertness, K. A.; Mansfield, L.; Schlager, J. B.; Sanders, A. W.; Roshko, A.; Burton, B. B.; George, S. M. Steady-State and Transient Photoconductivity in c-Axis GaN Nanowires Grown by Nitrogen-Plasma-Assisted Molecular Beam Epitaxy. *Journal of Applied Physics* **2010**, *107* (3), 034318. https://doi.org/10.1063/1.3275888.
(21) González-Posada, F.; Songmuang, R.; Den Hertog, M.; Monroy, E. Room-Temperature Photodetection Dynamics of Single GaN Nanowires. *Nano Lett.* **2012**, *12* (1), 172–176. https://doi.org/10.1021/nl2032684.
(22) González-Posada, F.; Songmuang, R.; Den Hertog, M.; Monroy, E. Environmental Sensitivity of *n-i-n* and Undoped Single GaN Nanowire Photodetectors. *Appl. Phys. Lett.* **2013**, *102* (21), 213113. https://doi.org/10.1063/1.4808017.
(23) Chen, R. S.; Tsai, H. Y.; Chan, C. H.; Huang, Y. S.; Chen, Y. T.; Chen, K. H.; Chen, L. C. Comparison of CVD- and MBE-Grown GaN Nanowires: Crystallinity, Photoluminescence, and Photoconductivity. *Journal of Elec Materi* **2014**, *44* (1), 177–187. https://doi.org/10.1007/s11664-014-3457-y.
(24) Lähnemann, J.; Den Hertog, M.; Hille, P.; de la Mata, M.; Fournier, T.; Schörmann, J.; Arbiol, J.; Eickhoff, M.; Monroy, E. UV Photosensing Characteristics of Nanowire-Based GaN/AlN Superlattices. *Nano Letters* **2016**, *16* (5), 3260–3267. https://doi.org/10.1021/acs.nanolett.6b00806.
(25) Spies, M.; Polaczyński, J.; Ajay, A.; Kalita, D.; Luong, M. A.; Lähnemann, J.; Gayral, B.; den Hertog, M. I.; Monroy, E. Effect of the Nanowire Diameter on the Linearity of the Response of GaN-Based Heterostructured Nanowire Photodetectors. *Nanotechnology* **2018**, *29* (25), 255204. https://doi.org/10.1088/1361-6528/aab838.
(26) Cuesta, S.; Spies, M.; Boureau, V.; Donatini, F.; Hocevar, M.; den Hertog, M. I.; Monroy, E. Effect of Bias on the Response of GaN Axial p–n Junction Single-Nanowire Photodetectors. *Nano Lett.* **2019**, *19* (8), 5506–5514. https://doi.org/10.1021/acs.nanolett.9b02040.
(27) Aiello, A.; Wu, Y.; Mi, Z.; Bhattacharya, P. Deep Ultraviolet Monolayer GaN/AlN Disk-in-Nanowire Array Photodiode on Silicon. *Appl. Phys. Lett.* **2020**, *116* (6), 061104. https://doi.org/10.1063/1.5135570.
(28) Han, S.; Noh, S.; Kim, J.-W.; Lee, C.-R.; Lee, S.-K.; Kim, J. S. Stretchable Inorganic GaN-Nanowire Photosensor with High Photocurrent and Photoresponsivity. *ACS Appl. Mater. Interfaces* **2021**, *13* (19), 22728–22737. https://doi.org/10.1021/acsami.1c03023.
(29) Le, B. H.; Zhao, S.; Liu, X.; Woo, S. Y.; Botton, G. A.; Mi, Z. Controlled Coalescence of AlGaN Nanowire Arrays: An Architecture for Nearly Dislocation-Free Planar Ultraviolet Photonic Device Applications. *Adv. Mater.* **2016**, *28* (38), 8446–8454. https://doi.org/10.1002/adma.201602645.
(30) Goswami, L. Fabrication of GaN Nano-Towers Based Self-Powered UV Photodetector. *Scientific Reports* **2021**, 10.

(31) Reddeppa, M.; Park, B.-G.; Pasupuleti, K. S.; Nam, D.-J.; Kim, S.-G.; Oh, J.-E.; Kim, M.-D. Current–Voltage Characteristics and Deep-Level Study of GaN Nanorod Schottky-Diode-Based Photodetector. *Semicond. Sci. Technol.* **2021**, *36* (3), 035010. https://doi.org/10.1088/1361-6641/abda62.

(32) Janjua, B.; Sun, H.; Zhao, C.; Anjum, D. H.; Wu, F.; Alhamoud, A. A.; Li, X.; Albadri, A. M.; Alyamani, A. Y.; El-Desouki, M. M.; Ng, T. K.; Ooi, B. S. Self-Planarized Quantum-Disks-in-Nanowires Ultraviolet-B Emitters Utilizing Pendeo-Epitaxy. *Nanoscale* **2017**, *9* (23), 7805–7813. https://doi.org/10.1039/C7NR00006E.

(33) Høiaas, I. M.; Liudi Mulyo, A.; Vullum, P. E.; Kim, D.-C.; Ahtapodov, L.; Fimland, B.-O.; Kishino, K.; Weman, H. GaN/AlGaN Nanocolumn Ultraviolet Light-Emitting Diode Using Double-Layer Graphene as Substrate and Transparent Electrode. *Nano Lett.* **2019**, *19* (3), 1649–1658. https://doi.org/10.1021/acs.nanolett.8b04607.

(34) Nguyen, H. P. T.; Zhang, S.; Cui, K.; Han, X.; Fathololoumi, S.; Couillard, M.; Botton, G. A.; Mi, Z. P-Type Modulation Doped InGaN/GaN Dot-in-a-Wire White-Light-Emitting Diodes Monolithically Grown on Si(111). *Nano Lett.* **2011**, *11* (5), 1919–1924. https://doi.org/10.1021/nl104536x.

(35) Ra, Y.; Lee, C. Monolithic Light Reflector-Nanowire Light Emitting Diodes. *Adv Materials Technologies* **2021**, *6* (2), 2000885. https://doi.org/10.1002/admt.202000885.

(36) Aiello, A.; Hoque, A. K. M. H.; Baten, M. Z.; Bhattacharya, P. High-Gain Silicon-Based InGaN/GaN Dot-in-Nanowire Array Photodetector. *ACS Photonics* **2019**, *6* (5), 1289–1294. https://doi.org/10.1021/acsphotonics.9b00390.

(37) Haggren, T.; Shah, A.; Autere, A.; Kakko, J.-P.; Dhaka, V.; Kim, M.; Huhtio, T.; Sun, Z.; Lipsanen, H. Nanowire Encapsulation with Polymer for Electrical Isolation and Enhanced Optical Properties. *Nano Res.* **2017**, *10* (8), 2657–2666. https://doi.org/10.1007/s12274-017-1468-8.

(38) Zhang, H.; Dai, X.; Guan, N.; Messanvi, A.; Neplokh, V.; Piazza, V.; Vallo, M.; Bougerol, C.; Julien, F. H.; Babichev, A.; Cavassilas, N.; Bescond, M.; Michelini, F.; Foldyna, M.; Gautier, E.; Durand, C.; Eymery, J.; Tchernycheva, M. Flexible Photodiodes Based on Nitride Core/Shell p–n Junction Nanowires. *ACS Appl. Mater. Interfaces* **2016**, *8* (39), 26198–26206. https://doi.org/10.1021/acsami.6b06414.

(39) Hartensveld, M.; Zhang, J. Monolithic Integration of GaN Nanowire Light-Emitting Diode With Field Effect Transistor. *IEEE Electron Device Lett.* **2019**, *40* (3), 427–430. https://doi.org/10.1109/LED.2019.2895846.

(40) de Luna Bugallo, A.; Tchernycheva, M.; Jacopin, G.; Rigutti, L.; Julien, F. H.; Chou, S.-T.; Lin, Y.-T.; Tseng, P.-H.; Tu, L.-W. Visible-Blind Photodetector Based on p–i–n Junction GaN Nanowire Ensembles. *Nanotechnology* **2010**, *21* (31), 315201. https://doi.org/10.1088/0957-4484/21/31/315201.

(41) Babichev, A. V.; Zhang, H.; Lavenus, P.; Julien, F. H.; Egorov, A. Yu.; Lin, Y. T.; Tu, L. W.; Tchernycheva, M. GaN Nanowire Ultraviolet Photodetector with a Graphene Transparent Contact. *Appl. Phys. Lett.* **2013**, *103* (20), 201103. https://doi.org/10.1063/1.4829756.

(42) Zhang, H.; Guan, N.; Piazza, V.; Kapoor, A.; Bougerol, C.; Julien, F. H.; Babichev, A. V.; Cavassilas, N.; Bescond, M.; Michelini, F.; Foldyna, M.; Gautier, E.; Durand, C.; Eymery, J.; Tchernycheva, M. Comprehensive Analyses of Core–Shell InGaN/GaN Single Nanowire Photodiodes. *J. Phys. D: Appl. Phys.* **2017**, *50* (48), 484001. https://doi.org/10.1088/1361-6463/aa935d.

(43) Hackett, L. P.; Seyedi, M. A.; Fiorentino, M.; Beausoleil, R. G. Large-Area Silicon Nanowire Schottky Junction Photodetector with Tunable Absorption and Low Junction Capacitance. *J. Phys. D: Appl. Phys.* **2017**, *50* (21), 215105. https://doi.org/10.1088/1361-6463/aa6d21.
(44) Shao, Y.; Pala, M.; Esseni, D.; del Alamo, J. A. Scaling of GaSb/InAs Vertical Nanowire Esaki Diodes Down to Sub-10-Nm Diameter. *IEEE Trans. Electron Devices* **2022**, *69* (4), 2188–2195. https://doi.org/10.1109/TED.2022.3145767.
(45) Jacopin, G.; De Luna Bugallo, A.; Rigutti, L.; Lavenus, P.; Julien, F. H.; Lin, Y.-T.; Tu, L.-W.; Tchernycheva, M. Interplay of the Photovoltaic and Photoconductive Operation Modes in Visible-Blind Photodetectors Based on Axial p-i-n Junction GaN Nanowires. *Appl. Phys. Lett.* **2014**, *104* (2), 023116. https://doi.org/10.1063/1.4860968.
(46) Sanchez-Garcia, M. A.; Calleja, E.; Monroy, E.; Sanchez, F. J.; Calle, F.; Muñoz, E.; Beresford, R. The Effect of the III/V Ratio and Substrate Temperature on the Morphology and Properties of GaN- and AlN-Layers Grown by Molecular Beam Epitaxy on Si(1 1 1). *Journal of Crystal Growth* **1998**, *183* (1–2), 23–30. https://doi.org/10.1016/S0022-0248(97)00386-2.
(47) Yoshizawa, M.; Kikuchi, A.; Mori, M.; Fujita, N.; Kishino, K. Growth of Self-Organized GaN Nanostructures on Al2O3(0001) by RF-Radical Source Molecular Beam Epitaxy. *Jpn. J. Appl. Phys.* **1997**, *36* (4B), L459. https://doi.org/10.1143/JJAP.36.L459.
(48) Ajay, A.; Lim, C. B.; Browne, D. A.; Polaczynski, J.; Bellet-Amalric, E.; den Hertog, M. I.; Monroy, E. Intersubband Absorption in Si- and Ge-Doped GaN/AlN Heterostructures in Self-Assembled Nanowire and 2D Layers. *physica status solidi (b)* **2017**, *254* (8), 1600734. https://doi.org/10.1002/pssb.201600734.
(49) Musolino, M.; Tahraoui, A.; Fernández-Garrido, S.; Brandt, O.; Trampert, A.; Geelhaar, L.; Riechert, H. Compatibility of the Selective Area Growth of GaN Nanowires on AlN-Buffered Si Substrates with the Operation of Light Emitting Diodes. *Nanotechnology* **2015**, *26* (8), 085605. https://doi.org/10.1088/0957-4484/26/8/085605.
(50) Dimkou, I.; Harikumar, A.; Donatini, F.; Lähnemann, J.; den Hertog, M. I.; Bougerol, C.; Bellet-Amalric, E.; Mollard, N.; Ajay, A.; Ledoux, G.; Purcell, S. T.; Monroy, E. Assessment of AlGaN/AlN Superlattices on GaN Nanowires as Active Region of Electron-Pumped Ultraviolet Sources. *Nanotechnology* **2020**, *31* (20), 204001. https://doi.org/10.1088/1361-6528/ab704d.
(51) Consonni, V.; Knelangen, M.; Geelhaar, L.; Trampert, A.; Riechert, H. Nucleation Mechanisms of Epitaxial GaN Nanowires: Origin of Their Self-Induced Formation and Initial Radius. *Phys. Rev. B* **2010**, *81* (8), 085310. https://doi.org/10.1103/PhysRevB.81.085310.
(52) Hille, P.; Müßener, J.; Becker, P.; de la Mata, M.; Rosemann, N.; Magén, C.; Arbiol, J.; Teubert, J.; Chatterjee, S.; Schörmann, J.; Eickhoff, M. Screening of the Quantum-Confined Stark Effect in AlN/GaN Nanowire Superlattices by Germanium Doping. *Applied Physics Letters* **2014**, *104* (10), 102104. https://doi.org/10.1063/1.4868411.
(53) Ajay, A.; Lim, C. B.; Browne, D. A.; Polaczyński, J.; Bellet-Amalric, E.; Bleuse, J.; den Hertog, M. I.; Monroy, E. Effect of Doping on the Intersubband Absorption in Si- and Ge-Doped GaN/AlN Heterostructures. *Nanotechnology* **2017**, *28* (40), 405204. https://doi.org/10.1088/1361-6528/aa8504.
(54) Robin, E. Method for the Determination of the Mass Thickness and the Composition of a Zone of an Object Using an Electron Beam and Measurements of X-Ray Intensities. EP3032244B1, August 2, 2017.

(55) Robin, E.; Mollard, N.; Guilloy, K.; Pauc, N.; Gentile, P.; Fang, Z.; Daudin, B.; Amichi, L.; Jouneau, P.-H.; Bougerol, C.; Delalande, M.; Bavencove, A.-L. Quantification of Dopants in Nanomaterial by SEM/EDS. In *European Microscopy Congress 2016: Proceedings*; European Microscopy Society, Ed.; Wiley-VCH Verlag GmbH & Co. KGaA: Weinheim, Germany, 2016; pp 380–381. https://doi.org/10.1002/9783527808465.EMC2016.6335.
(56) Bougerol, C.; Robin, E.; Di Russo, E.; Bellet-Amalric, E.; Grenier, V.; Ajay, A.; Rigutti, L.; Monroy, E. Solubility Limit of Ge Dopants in AlGaN: A Chemical and Microstructural Investigation Down to the Nanoscale. *ACS Appl. Mater. Interfaces* **2021**, *13* (3), 4165–4173. https://doi.org/10.1021/acsami.0c19174.
(57) Sabelfeld, K. K.; Kaganer, V. M.; Limbach, F.; Dogan, P.; Brandt, O.; Geelhaar, L.; Riechert, H. Height Self-Equilibration during the Growth of Dense Nanowire Ensembles: Order Emerging from Disorder. *Appl. Phys. Lett.* **2013**, *103* (13), 133105. https://doi.org/10.1063/1.4822110.
(58) Songmuang, R.; Ben, T.; Daudin, B.; González, D.; Monroy, E. Identification of III–N Nanowire Growth Kinetics via a Marker Technique. *Nanotechnology* **2010**, *21* (29), 295605. https://doi.org/10.1088/0957-4484/21/29/295605.
(59) Guerfi, Y.; Doucet, J. B.; Larrieu, G. Thin-Dielectric-Layer Engineering for 3D Nanostructure Integration Using an Innovative Planarization Approach. *Nanotechnology* **2015**, *26* (42), 425302. https://doi.org/10.1088/0957-4484/26/42/425302.
(60) Chia, A. C. E.; LaPierre, R. R. Contact Planarization of Ensemble Nanowires. *Nanotechnology* **2011**, *22* (24), 245304. https://doi.org/10.1088/0957-4484/22/24/245304.
(61) Kawashima, T.; Yoshikawa, H.; Adachi, S.; Fuke, S.; Ohtsuka, K. Optical Properties of Hexagonal GaN. *Journal of Applied Physics* **1997**, *82* (7), 3528–3535. https://doi.org/10.1063/1.365671.
(62) Calle, F.; Sánchez, F. J.; Tijero, J. M. G.; Sánchez-García, M. A.; Calleja, E.; Beresford, R. Exciton and Donor - Acceptor Recombination in Undoped GaN on Si(111). *Semiconductor Science and Technology* **1997**, *12* (11), 1396–1403. https://doi.org/10.1088/0268-1242/12/11/011.
(63) Almokhtar, M.; All, N. A.; Almarashi, J. Q. M.; Asahi, H. Photoluminescence Enhancement Associated with the Small Size of GaN Nanorods. *Journal of Alloys and Compounds* **2022**, *894*, 162408. https://doi.org/10.1016/j.jallcom.2021.162408.
(64) Shikanai, A.; Azuhata, T.; Sota, T.; Chichibu, S.; Kuramata, A.; Horino, K.; Nakamura, S. Biaxial Strain Dependence of Exciton Resonance Energies in Wurtzite GaN. *Journal of Applied Physics* **1997**, *81* (1), 417–424. https://doi.org/10.1063/1.364074.
(65) Hugues, M.; Shields, P. A.; Sacconi, F.; Mexis, M.; Auf der Maur, M.; Cooke, M.; Dineen, M.; Di Carlo, A.; Allsopp, D. W. E.; Zúñiga-Pérez, J. Strain Evolution in GaN Nanowires: From Free-Surface Objects to Coalesced Templates. *Journal of Applied Physics* **2013**, *114* (8), 084307. https://doi.org/10.1063/1.4818962.
(66) Yan, Q.; Rinke, P.; Janotti, A.; Scheffler, M.; Van de Walle, C. G. Effects of Strain on the Band Structure of Group-III Nitrides. *Phys. Rev. B* **2014**, *90* (12), 125118. https://doi.org/10.1103/PhysRevB.90.125118.
(67) Brandt, O.; Pfüller, C.; Chèze, C.; Geelhaar, L.; Riechert, H. Sub-MeV Linewidth of Excitonic Luminescence in Single GaN Nanowires: Direct Evidence for Surface Excitons. *Phys. Rev. B* **2010**, *81* (4), 045302. https://doi.org/10.1103/PhysRevB.81.045302.

(68) Korona, K. P.; Reszka, A.; Sobanska, M.; Perkowska, P. S.; Wysmołek, A.; Klosek, K.; Zytkiewicz, Z. R. Dynamics of Stacking Faults Luminescence in GaN/Si Nanowires. *Journal of Luminescence* **2014**, *155*, 293–297. https://doi.org/10.1016/j.jlumin.2014.06.061.
(69) Nogues, G.; Auzelle, T.; Den Hertog, M.; Gayral, B.; Daudin, B. Cathodoluminescence of Stacking Fault Bound Excitons for Local Probing of the Exciton Diffusion Length in Single GaN Nanowires. *Appl. Phys. Lett.* **2014**, *104* (10), 102102. https://doi.org/10.1063/1.4868131.
(70) Schmitz, A. C.; Ping, A. T.; Khan, M. A.; Chen, Q.; Yang, J. W.; Adesida, I. Metal Contacts to N-Type GaN. *Journal of Elec Materi* **1998**, *27* (4), 255–260. https://doi.org/10.1007/s11664-998-0396-5.
(71) Calarco, R.; Marso, M.; Richter, T.; Aykanat, A. I.; Meijers, R.; v.d. Hart, A.; Stoica, T.; Lüth, H. Size-Dependent Photoconductivity in MBE-Grown GaN−Nanowires. *Nano Lett.* **2005**, *5* (5), 981–984. https://doi.org/10.1021/nl0500306.
(72) Monroy, E.; Calle, F.; Garrido, J. A.; Youinou, P.; Muñoz, E.; Omnès, F.; Beaumont, B.; Gibart, P. Si-Doped Al $_x$ Ga $_{1-x}$ N Photoconductive Detectors. *Semicond. Sci. Technol.* **1999**, *14* (8), 685–689. https://doi.org/10.1088/0268-1242/14/8/303.
(73) Richter, T.; Meijers, H. L. R.; Calarco, R.; Marso, M. Doping Concentration of GaN Nanowires Determined by Opto-Electrical Measurements. *Nano Lett.* **2008**, *8* (9), 3056–3059. https://doi.org/10.1021/nl8014395.
(74) Birner, S.; Zibold, T.; Andlauer, T.; Kubis, T.; Sabathil, M.; Trellakis, A.; Vogl, P. Nextnano: General Purpose 3-D Simulations. *IEEE Transactions on Electron Devices* **2007**, *54* (9), 2137–2142. https://doi.org/10.1109/TED.2007.902871.
(75) Kandaswamy, P. K.; Bougerol, C.; Jalabert, D.; Ruterana, P.; Monroy, E. Strain Relaxation in Short-Period Polar GaN/AlN Superlattices. *Journal of Applied Physics* **2009**, *106* (1), 013526. https://doi.org/10.1063/1.3168431.
(76) Spies, M.; den Hertog, M. I.; Hille, P.; Schörmann, J.; Polaczyński, J.; Gayral, B.; Eickhoff, M.; Monroy, E.; Lähnemann, J. Bias-Controlled Spectral Response in GaN/AlN Single-Nanowire Ultraviolet Photodetectors. *Nano Lett.* **2017**, *17* (7), 4231–4239. https://doi.org/10.1021/acs.nanolett.7b01118.
(77) Rigutti, L.; Tchernycheva, M.; De Luna Bugallo, A.; Jacopin, G.; Julien, F. H.; Zagonel, L. F.; March, K.; Stephan, O.; Kociak, M.; Songmuang, R. Ultraviolet Photodetector Based on GaN/AlN Quantum Disks in a Single Nanowire. *Nano Lett.* **2010**, *10* (8), 2939–2943. https://doi.org/10.1021/nl1010977.
(78) Letov, V.; Perera, A. G. U.; Ershov, M.; Liu, H. C.; Buchanan, M.; Wasilewski, Z. R. Experimental Observation of Transient Photocurrent Overshoot in Quantum Well Infrared Photodetectors. *Infrared Physics & Technology* **2001**, *42* (3–5), 243–247. https://doi.org/10.1016/S1350-4495(01)00082-2.
(79) Bertelli, M.; Löptien, P.; Wenderoth, M.; Rizzi, A.; Ulbrich, R. G.; Righi, M. C.; Ferretti, A.; Martin-Samos, L.; Bertoni, C. M.; Catellani, A. Atomic and Electronic Structure of the Nonpolar GaN (1-100) Surface. *Phys. Rev. B* **2009**, *80* (11), 115324. https://doi.org/10.1103/PhysRevB.80.115324.
(80) OSI Systems Company, O. O. *Inversion Layer UV Enhanced Photodiodes UV-001*. https://www.osioptoelectronics.com/media/pages/products/photodetectors/uv-enhanced-100-qe/uv-20/69ace8f51b-1675100384/uv-enhanced-inversion-layer-photodiodes.pdf.
(81) Electro Optical Components, Inc. *GaP-Photodiode-JEP-365*. https://eoc-inc.com/wp-content/uploads/JEP1-JEP5-1.pdf.

(82) Zheng, Y.; Cao, B.; Tang, X.; Wu, Q.; Wang, W.; Li, G. Vertical 1D/2D Heterojunction Architectures for Self-Powered Photodetection Application: GaN Nanorods Grown on Transition Metal Dichalcogenides. *ACS Nano* **2022**, *16* (2), 2798–2810. https://doi.org/10.1021/acsnano.1c09791.
(83) Pasupuleti, K. S.; Reddeppa, M.; Park, B.-G.; Peta, K. R.; Oh, J.-E.; Kim, S.-G.; Kim, M.-D. Ag Nanowire-Plasmonic-Assisted Charge Separation in Hybrid Heterojunctions of Ppy-PEDOT:PSS/GaN Nanorods for Enhanced UV Photodetection. *ACS Appl. Mater. Interfaces* **2020**, *12* (48), 54181–54190. https://doi.org/10.1021/acsami.0c16795.
(84) Soci, C.; Zhang, A.; Xiang, B.; Dayeh, S. A.; Aplin, D. P. R.; Park, J.; Bao, X. Y.; Lo, Y. H.; Wang, D. ZnO Nanowire UV Photodetectors with High Internal Gain. *Nano Lett.* **2007**, *7* (4), 1003–1009. https://doi.org/10.1021/nl070111x.
(85) Sarkar, N.; Dhar, S.; Ghosh, S. The Role of the Grain Boundary on Persistent Photoconductivity in GaN. *J. Phys.: Condens. Matter* **2003**, *15* (43), 7325–7335. https://doi.org/10.1088/0953-8984/15/43/015.
(86) Koehler, A. D.; Anderson, T. J.; Khachatrian, A.; Nath, A.; Tadjer, M. J.; Buchner, S. P.; Hobart, K. D.; Kub, F. J. High Voltage GaN Lateral Photoconductive Semiconductor Switches. *ECS J. Solid State Sci. Technol.* **2017**, *6* (11), S3099–S3102. https://doi.org/10.1149/2.0231711jss.

Figures

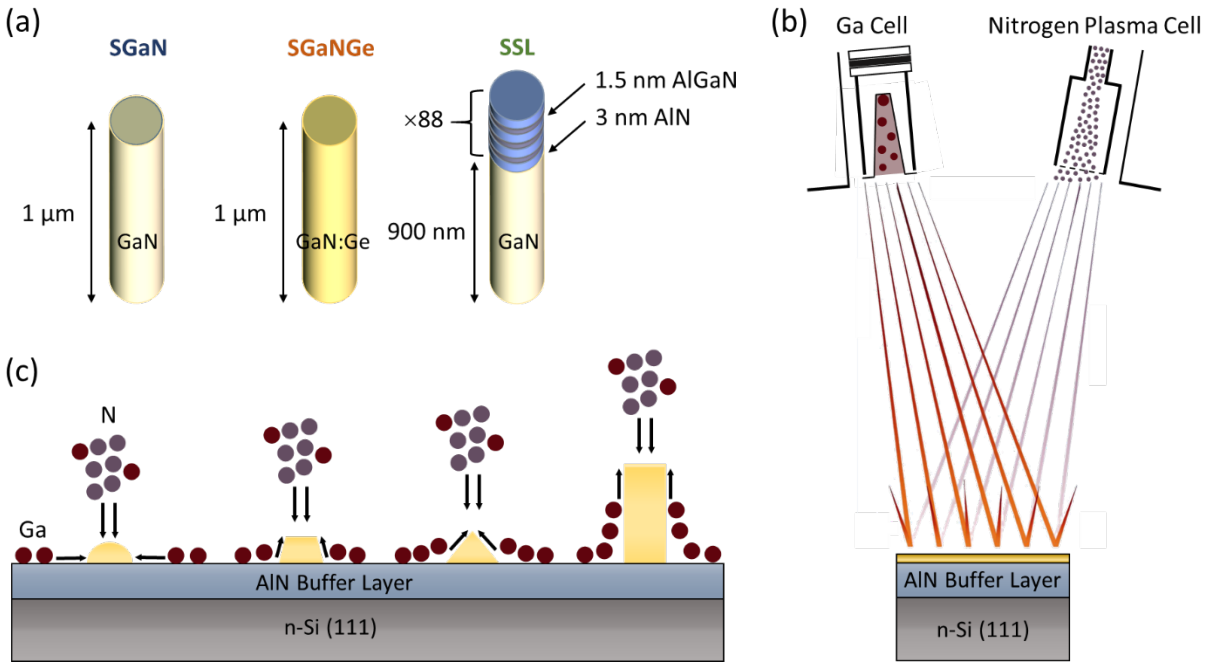

Figure 1. Schematic representation of (a) samples under study, nanowire growth process (b) MBE structure, and (c) nanowire nucleation mechanism.

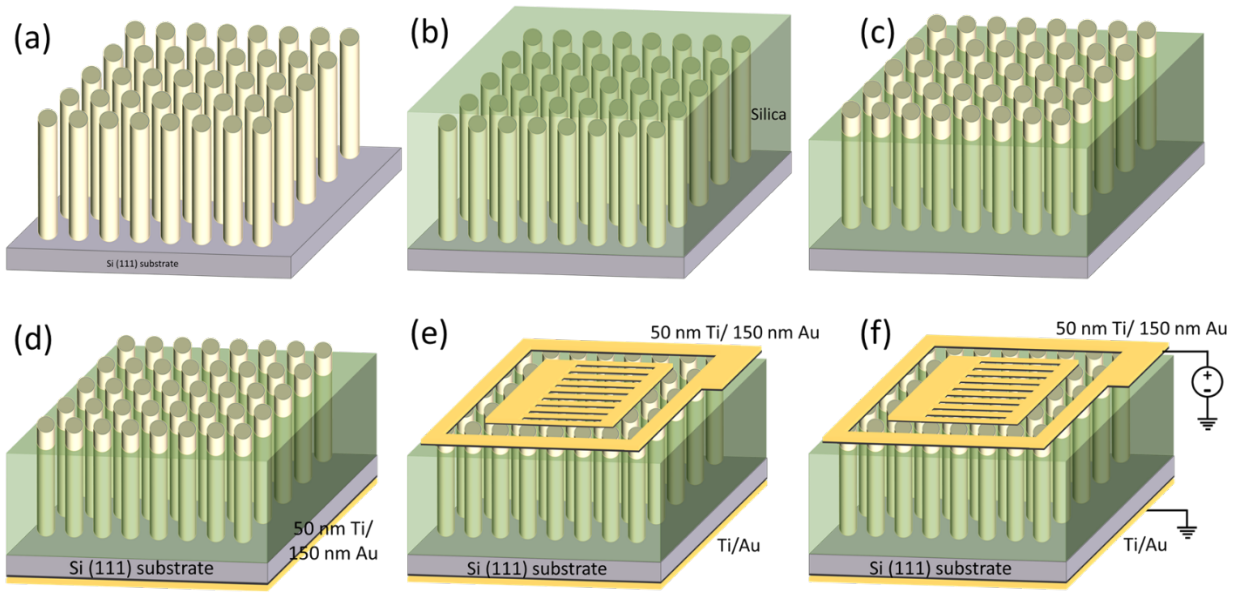

Figure 2. Schematic representation of the device fabrication steps: (a) As-grown nanowire sample, (b) planarization, (c) exposure of the nanowire tip after dry etching, (d) back contact on the silicon substrate, (e) first lithography and metallization to define the fingers and contact pad, and (f) second lithography and metallization to deposit a semi-transparent spread layer.

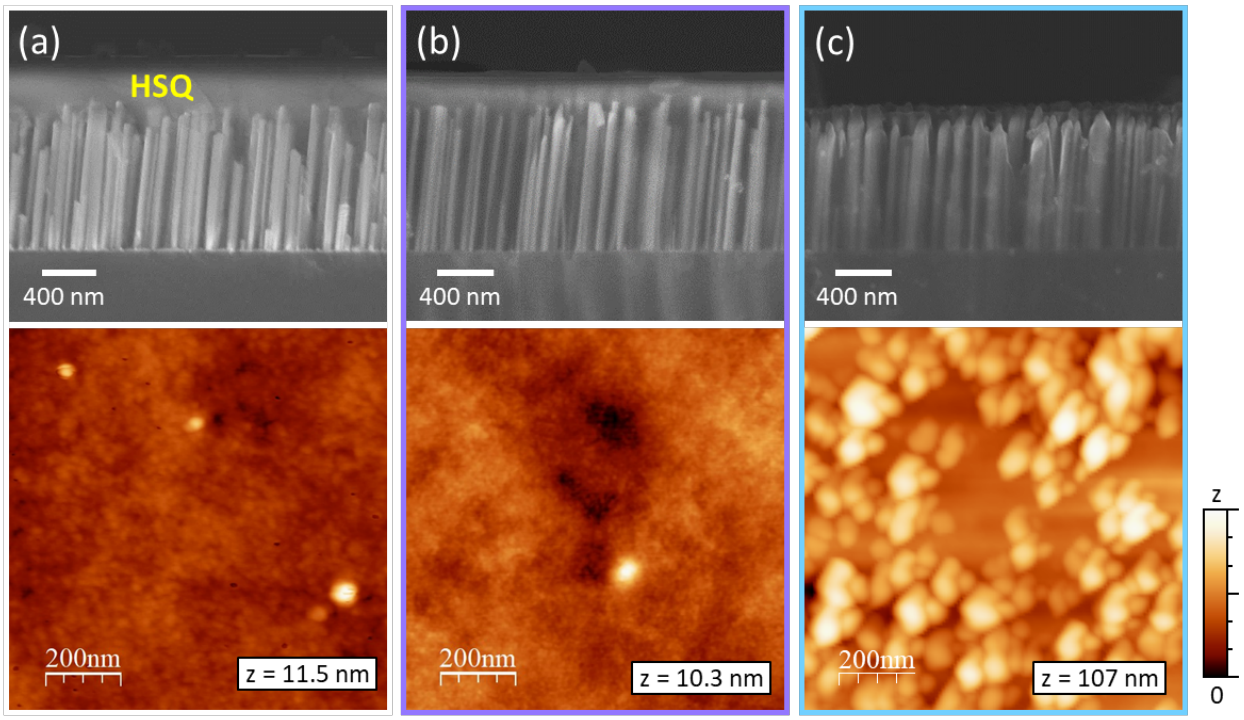

Figure 3. (Top) Cross-section SEM image and (bottom) AFM image of sample SGaN after planarization and (a) before SiO_2 etching, (b) after etching 150 nm of SiO_2 and (c) after etching 350 nm of SiO_2.

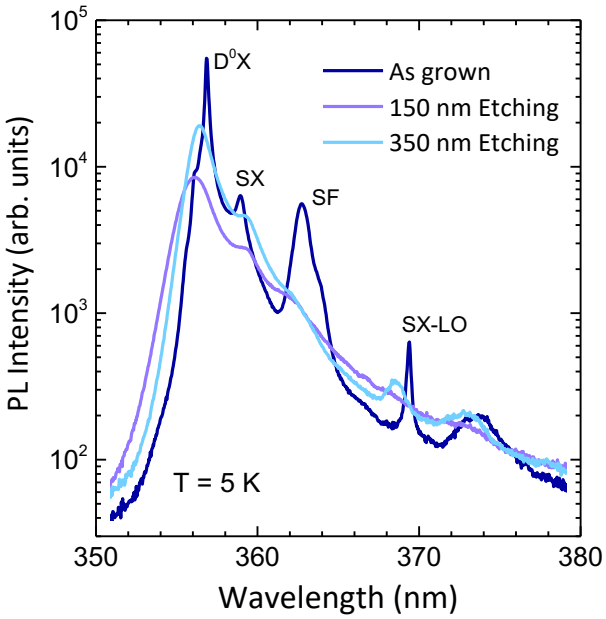

Figure 4. Low temperature (T = 5 K) PL spectrum of as-grown, 150-nm-etched and 350-nm-etched SGaN.

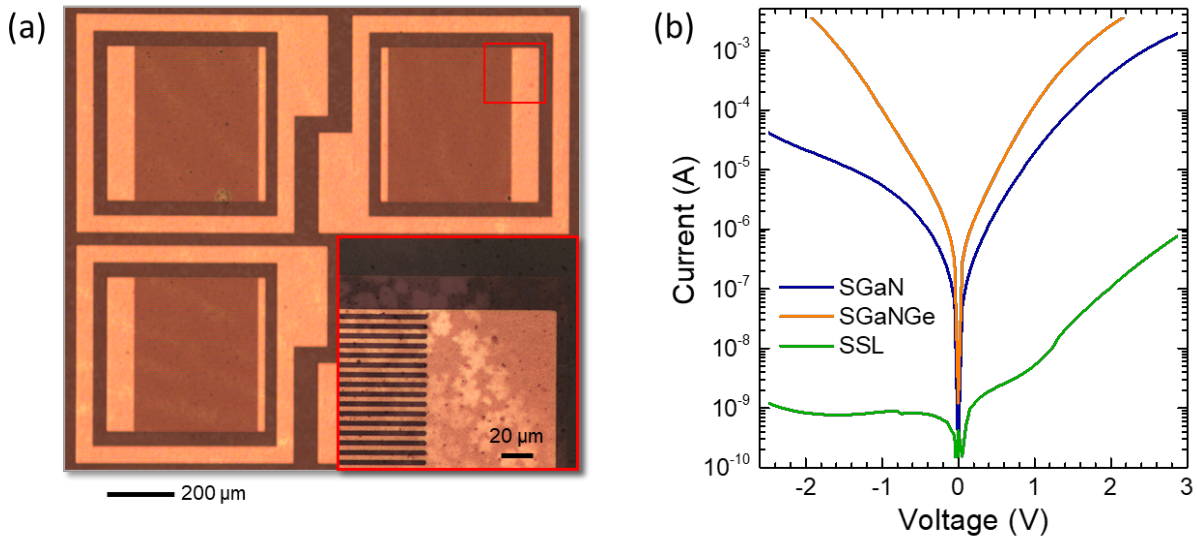

Figure 5. (a) Top view of the devices in an optical microscope, with a zoom on the fingers. (b) Current-voltage characteristics of samples SGaN, SGaNGe and SSL measured in the dark.

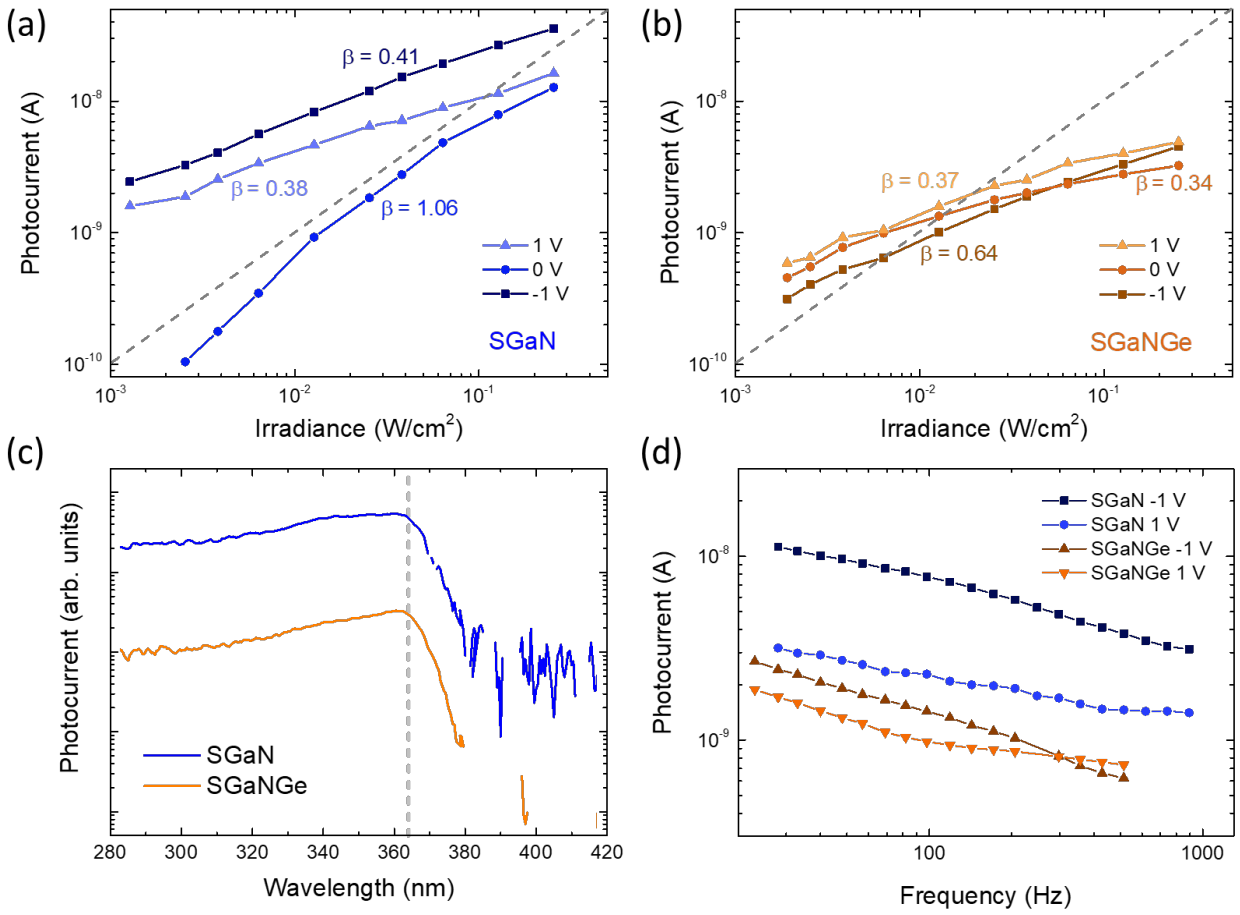

Figure 6. Variation of photocurrent (I_{ph}) as a function of impinging optical power (P_{opt}) at 325 nm (the slope for β = 1 (i.e., linear behavior) is represented by a gray dashed line) for (a) SGaN, (b) SGaNGe, comparison between SGaN and SGaNGe samples in terms of (c) spectral response measurement, and (d) variation of the photocurrent as a function of the chopping frequency (SGaN and SGaNGe are indicated with blue and orange color, respectively).

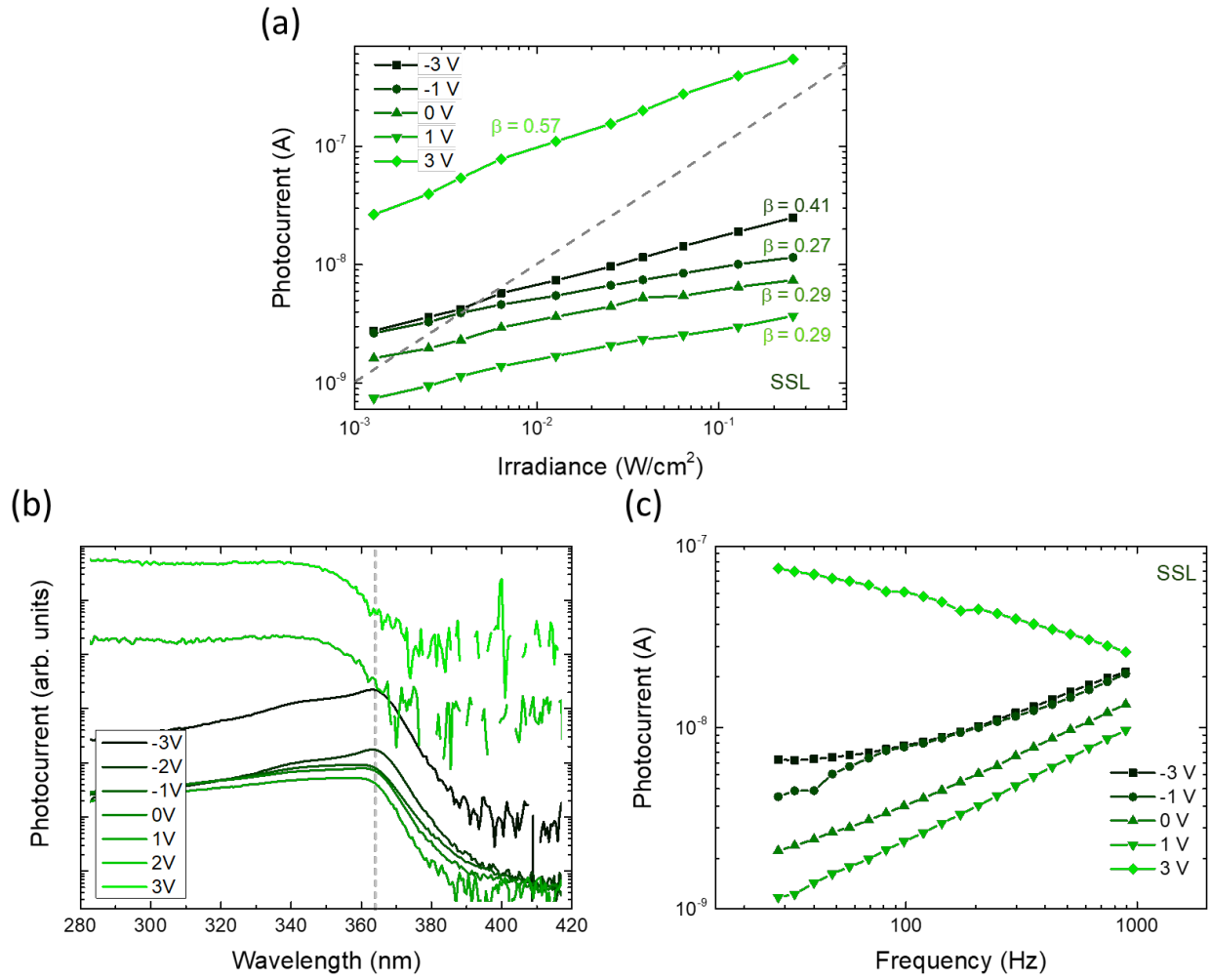

Figure 7. Optical measurements of sample SSL. (a) Variation of photocurrent (I_{ph}) as a function of impinging optical power (P_{opt}) at 325 nm (The slope for β=1 (i.e. linear behavior) is represented by a gray dashed line). (b) Spectral response (the gray dashed line indicates the wavelength of the GaN at room temperature), (c) Variation of the photocurrent as a function of the chopping frequency.

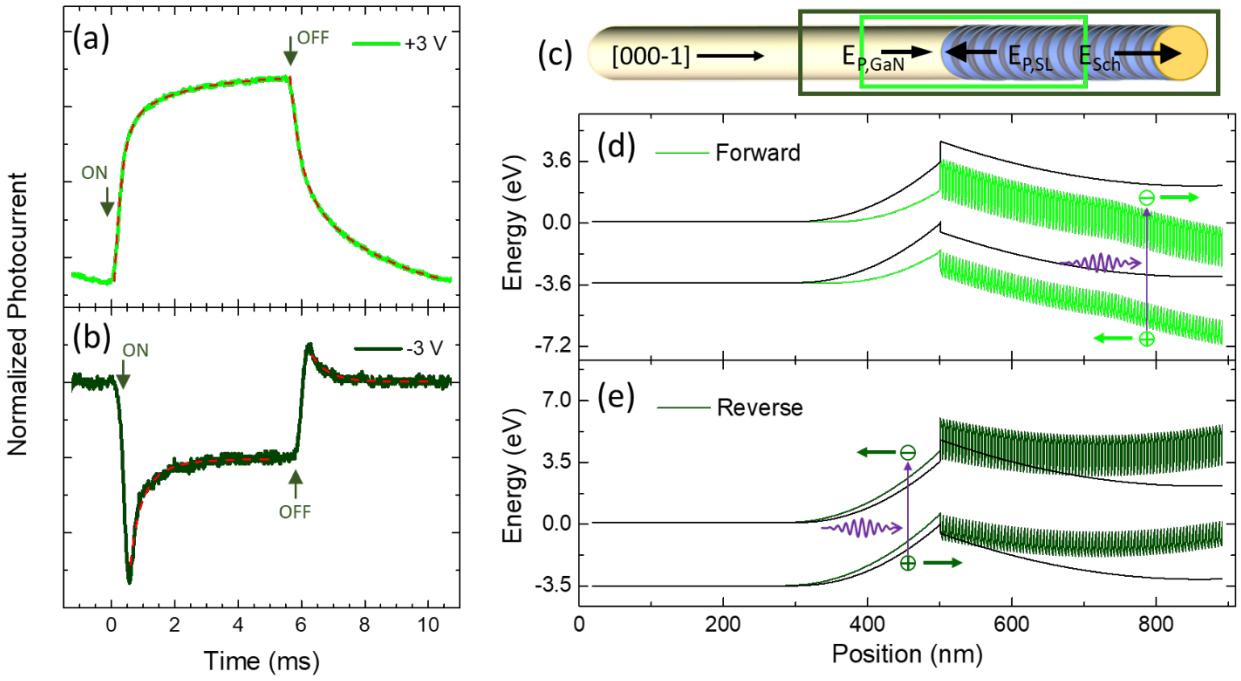

Figure 8. Rise and fall time of the photocurrent measured in the SSL sample at (a) +3 V and (b) -3 V. Dashed lines are biexponential fits. (c) Schematic representation of the SSL structure given with the internal electric field formations within the structure. (d,e) One-dimensional calculations of the SSL band structure along the growth axis under (d) forward and (e) reverse bias. The black band diagram corresponds to the potential profile of the nanowire structure under zero bias (the quantum wells were smoothed out in this reference profile).